

## PLANT SCIENCES

High-resolution cryo-EM structures of plant cytochrome  $b_6f$  at workMarcin Sarewicz<sup>1</sup>, Mateusz Szwalec<sup>1</sup>, Sebastian Pintscher<sup>1,2</sup>, Paulina Indyka<sup>2,3</sup>, Michał Rawski<sup>2</sup>, Rafał Pietras<sup>1</sup>, Bohun Mielecki<sup>1</sup>, Łukasz Koziej<sup>2</sup>, Marcin Jaciuk<sup>2</sup>, Sebastian Glatt<sup>2\*</sup>, Artur Osyczka<sup>1\*</sup>

Plants use solar energy to power cellular metabolism. The oxidation of plastoquinol and reduction of plastocyanin by cytochrome  $b_6f$  (Cyt  $b_6f$ ) is known as one of the key steps of photosynthesis, but the catalytic mechanism in the plastoquinone oxidation site ( $Q_p$ ) remains elusive. Here, we describe two high-resolution cryo-EM structures of the spinach Cyt  $b_6f$  homodimer with endogenous plastoquinones and in complex with plastocyanin. Three plastoquinones are visible and line up one after another head to tail near  $Q_p$  in both monomers, indicating the existence of a channel in each monomer. Therefore, quinones appear to flow through Cyt  $b_6f$  in one direction, transiently exposing the redox-active ring of quinone during catalysis. Our work proposes an unprecedented one-way traffic model that explains efficient quinol oxidation during photosynthesis and respiration.

## INTRODUCTION

Cytochromes bc (Cyt bc) are central components of cellular energy conversion systems (1–5). This large family of enzymes encompasses cytochromes  $bc_1$  (Cyt  $bc_1$ ) and cytochromes  $b_6f$  (Cyt  $b_6f$ ). Cyt  $bc_1$  in mitochondria links complexes I and II with complex IV, while Cyt  $b_6f$  in oxygenic photosynthesis couples photosystems I and II (PSI and PSII) (6, 7). Cyt bc oxidize quinols (plastoquinol, PQH<sub>2</sub> in chloroplasts) and reduce water-soluble electron carriers, like cytochrome c (Cyt c) or plastocyanin (PC). The electron transfer within Cyt bc is coupled to the translocation of protons across the membrane, which contributes to the generation of the proton motive force needed for adenosine 5'-triphosphate production (8). The so-called Q-cycle has been a useful framework to describe the catalytic activity of Cyt bc (9–13). The model is based on a coordinated action of two catalytic sites, namely,  $Q_p$  and  $Q_n$  (quinol oxidation and quinone reduction sites, respectively), which locate toward the positive and negative sides of the membrane, respectively, and are embedded in a network formed by a Rieske cluster (2Fe2S) and b- and c-type hemes. These sites interact with mobile pools of quinone/quinol molecules inside the membrane and Cyt c or PC outside the membrane (1, 2). This interaction not only secures energetic efficiency of the photosynthetic or respiratory chains but also can be modulated and regulated by various cellular processes. This kind of regulatory control mechanism seems to be of particular importance during photosynthesis, where Cyt  $b_6f$  can switch between linear electron transfer (LET) and cyclic electron transfer (CET) (Fig. 1A) or engage in photosynthetic state transitions (14–17). It is evident that understanding of all these processes requires a fundamental knowledge of how substrates enter and leave the respective catalytic sites. However, the characterization of these crucial reaction intermediates remains challenging, particularly with respect to  $Q_p$  for which the available structures of Cyt  $b_6f$  (18–20) did not disclose the position nor the orientation of the

natural substrate in the catalytic site. Plastoquinone (PQ) in this region was found only at the position proposed to represent a snapshot of its approach to  $Q_p$  (20). On the other hand, it was recognized that the specific inhibitors of  $Q_p$  occupy the well-defined positions at the site that gave rise to an assumption that these compounds mimic the interaction of the substrate in the catalytically active conformation (18, 19, 21).

Here, we embarked on a structural study of spinach Cyt  $b_6f$  in the presence and absence of PC to uncover a series of locations for the native PQ substrate around  $Q_p$ , as opposed to single locations characteristic for the  $Q_p$  inhibitors. These PQ molecules appear to form a chain, which suggests an unprecedented mode of interaction giving rise to an intriguing view of how quinones might pass through the enzyme. This has important consequences for the description of the individual steps of the catalytic Q cycle for the associated regulatory mechanisms of photosynthesis and for respiration in general. Our conclusions are based on two high-resolution single-particle cryo-electron microscopy (cryo-EM) reconstruction of enzymatically active Cyt  $b_6f$  isolated from native source.

## RESULTS AND DISCUSSION

Structure of spinach Cyt  $b_6f$  in complex with PC at 2.7 Å resolution

Our isolation protocol has been optimized to minimize purification steps and to prevent a loss of PQ throughout the procedure (see Protocol 1) (Fig. 1B). The detergent-solubilized Cyt  $b_6f$  complex was supplemented with a 2.5-fold molar excess of separately purified PC (fig. S1). Thereby, we resolved a nonsymmetrized structure of PC-bound Cyt  $b_6f$  at an overall resolution of 2.7 Å (Fig. 1, C and D, and table S1), with certain regions in the core reaching local resolutions of up to 2.1 Å. We used additional focused subclassification protocols to enhance the density of PC, which resulted in a similar reconstruction at a 3.2 Å resolution (fig. S2). The hydrophobic parts of the PC-bound Cyt  $b_6f$  homodimer, which are embedded in the thylakoid membrane, are surrounded by a mixture of ordered (fig. S3) and disordered lipids and detergent molecules (Fig. 1C). Each monomer of Cyt  $b_6f$  comprises eight subunits: Cyt f, Cyt  $b_6$ , subunit IV (SubIV), iron-sulfur protein (ISP), PetG, PetL, PetM, and PetN.

<sup>1</sup>Faculty of Biochemistry, Biophysics, and Biotechnology, Jagiellonian University, Kraków, Poland. <sup>2</sup>Małopolska Centre of Biotechnology (MCB), Jagiellonian University, Kraków, Poland. <sup>3</sup>National Synchrotron Radiation Centre SOLARIS, Jagiellonian University, Kraków, Poland.

\*Corresponding author. Email: sebastian.glatt@uj.edu.pl (S.G.) and artur.osyczka@uj.edu.pl (A.O.)

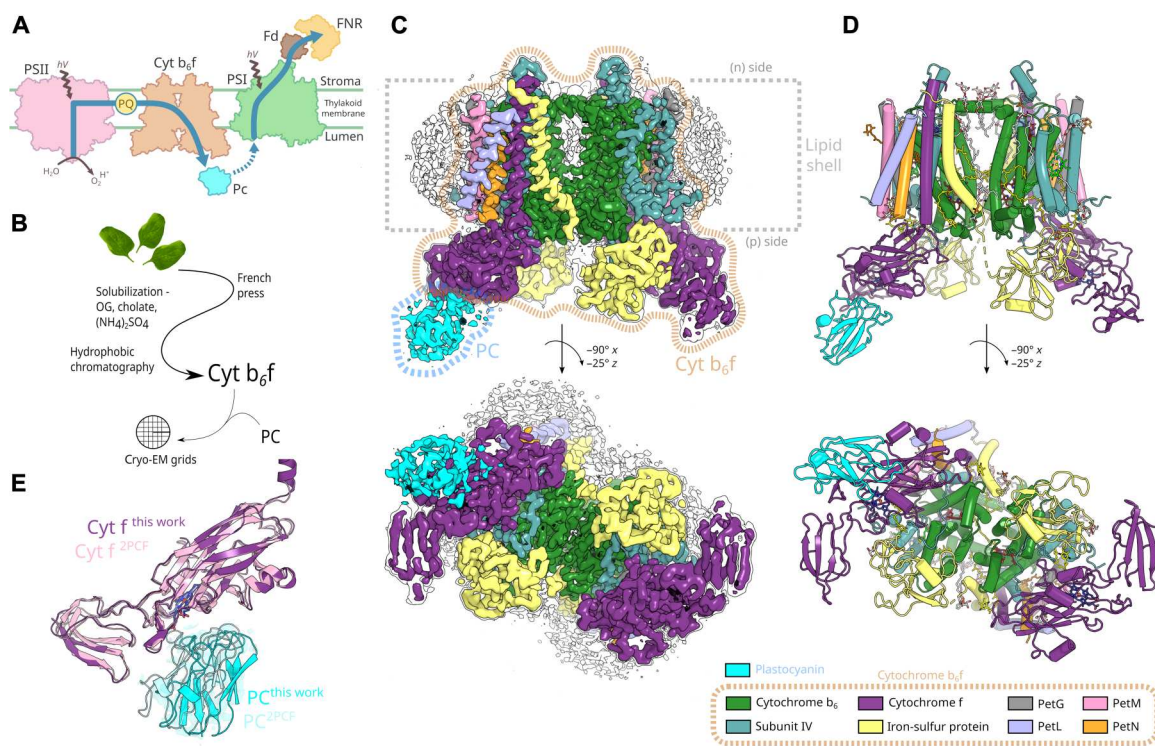


**Fig. 1. Overview of the structure and function of the Cyt  $b_6f$ -PC complex.** (A) Simplified scheme of LET with blue arrows showing the main route for electrons between proteins: PSII and PSI are operating in series, and Cyt  $b_6f$  provides a conduit for electron transfer between the two photosystems. Fd, ferredoxin; FNR, ferredoxin:NADP<sup>+</sup> reductase. During CET, electrons from PSI are used to reduce membranous PQ and Q<sub>n</sub>, of Cyt  $b_6f$  is one of the possible sites for this reduction. (B) Summary of crucial steps of Cyt  $b_6f$ -PC sample preparation. (C) Cryo-EM density map of the Cyt  $b_6f$ -PC complex oriented parallel (top) and perpendicular, as seen from the lumen side (bottom). Detergent molecules are shown in light gray. Cyt  $b_6f$  dimer and PC are outlined with dotted orange and blue lines, respectively. (D) Cartoon model of the Cyt  $b_6f$ -PC complex (PDB: 7QRM) presented in the same orientation as in (C). (E) Close-up view of the binding domain of PC bound to the water-soluble part of Cyt f, overlaid with a structure previously determined by NMR (PDB: 2PCF). The boxes show color codes used to indicate PC and subunits of Cyt  $b_6f$  in (C) and (D).

An additional density matching the size and shape of PC can be found next to the head domain of Cyt f in only one of the monomers, whereas the same position in the other monomer shows no signs of a bound PC molecule (Fig. 1C). The apparent asymmetric binding of PC might be caused by the low binding affinity and the highly dynamic and transient nature of the interaction (22–24). Such a diffusion-coupled mechanism of binding has been well documented for analogous interaction of Cyt c with Cyt  $bc_1$  (25, 26). Likewise, the crystal structure of yeast Cyt  $bc_1$  in complex with Cyt c also shows binding of the substrate only on one side of the dimer (27).

The mobility and dynamics of PC also results in a lower local resolution of PC compared to the surrounding Cyt  $b_6f$  core structure. Even after focused local classification and refinement steps, the individual secondary structure elements are barely distinguishable (fig. S2). Nonetheless, the density distribution around the copper coordination site appears stronger and allows us to unambiguously assign the orientation of bound PC. Notably, PC binds in an almost identical position as observed in the nuclear magnetic resonance (NMR) structure of turnip Cyt f and spinach PC [Protein Data Bank (PDB): 2PCF] (Fig. 1E), which also showed local movements of bound PC (22). All possible conformations bring copper and c-type heme f of Cyt f at a distance of 12.4 Å to support fast interprotein electron transfer (Fig. 2). The binding of PC did not cause any

detectable structural change in the Cyt  $b_6f$  core subunits. Thus, the recruitment and binding of PC is mediated by local interactions and does not induce major domain rearrangements in Cyt  $b_6f$ .

### Cryo-EM structure of spinach Cyt $b_6f$ at 2.1 Å resolution

Our reconstitution and structural characterization of the Cyt  $b_6f$ -PC complex was followed by a similar analysis of Cyt  $b_6f$ , isolated independently using a protocol with additional modifications (see Protocol 2) but without adding PC. We collected a second large cryo-EM dataset and, after applying C2 symmetry, were able to obtain a reconstruction at an overall resolution of 2.1 Å, with certain regions in the core reaching local resolutions of up to 1.9 Å. The high quality of the obtained density map (Fig. 3A) allows for unambiguous identification of amino acid side chains as exemplified by one of the helices and the highly conserved Pro-Glu-Trp-Tyr (PEWY) sequence of Q<sub>p</sub> in SubIV (Fig. 3B) (28). The reconstruction also shows the positions of the redox-active cofactors, namely, a pair of heme  $b_n$  and  $c_n$  bridged by a water molecule or hydroxyl anion (Fig. 3C) (29); heme  $b_p$  (Fig. 3D); 2Fe2S ligated by Cys<sup>107</sup>, Cys<sup>125</sup>, His<sup>109</sup>, and His<sup>128</sup> (Fig. 3E); and heme f (Fig. 3F). Overall, the arrangement, coordination patterns, and relative intermolecular distances of the cofactors are as in the Cyt  $b_6f$ -PC complex at 2.7 Å (Figs. 1) and 2. They are similar to the previously described crystal structures of Cyt  $b_6f$  (18, 19, 30) and the lower-

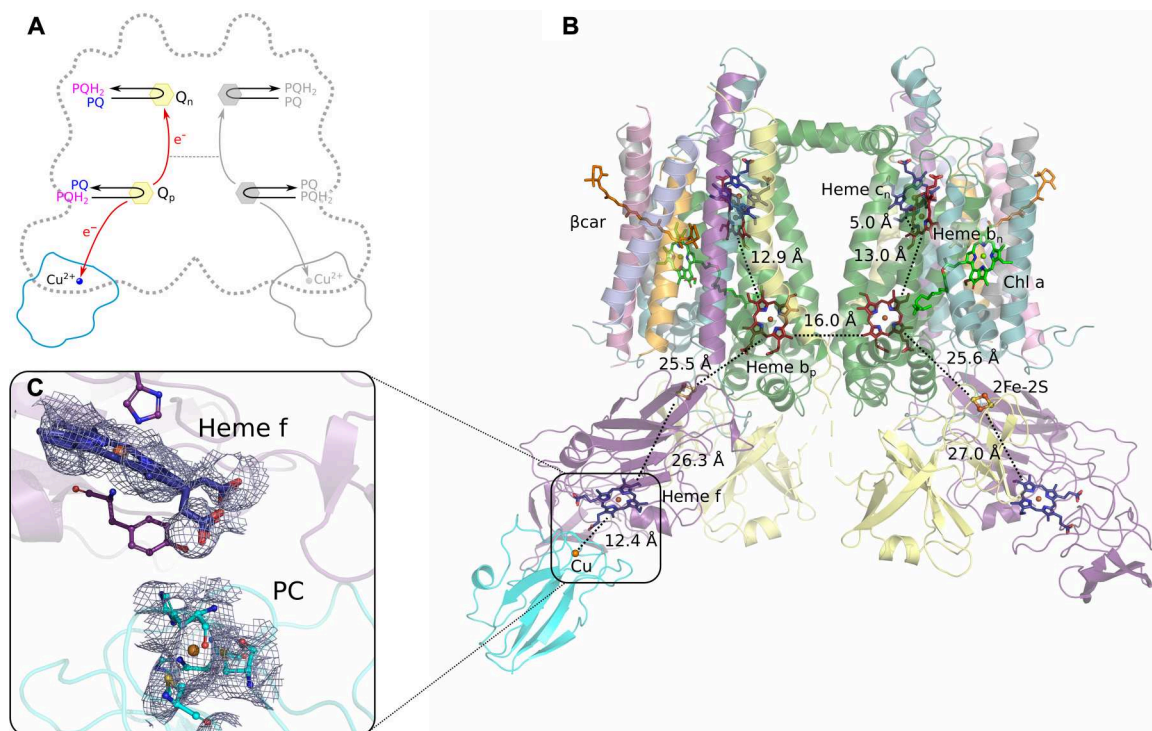


**Fig. 2. Overview of prosthetic groups and catalytic sites in the Cyt  $b_6f$ -PC complex.** (A) Simplified scheme showing the positions of  $Q_p$  and  $Q_n$  on the protein contour taken from (B) and the overall directions of the  $PQH_2$ / $PQ$  catalytic reactions (black arrows) and the electron transfers (red arrows). (B) Arrangement of prosthetic groups and the distances between the redox-active cofactors (hemes and 2Fe2S). (C) Close-up view on the structure of heme  $f$  and  $Cu^{2+}$  ion.

resolution cryo-EM structure of spinach Cyt  $b_6f$  (20). This arrangement is highly conserved throughout all Cyts  $bc$  and features characteristic assembly of the cofactors into two separate chains with the  $Q_p$  acting as the branch point for them. Such a separation is necessary to secure a bifurcation reaction (BR) upon which quinol is oxidized at  $Q_p$ . During the BR, one electron deriving from  $PQH_2$  is transferred through the 2Fe2S and heme  $f$  to reduce PC. The other electron is transferred through heme  $b_p$  and a pair of hemes  $b_n$  and  $c_n$  to ultimately reduce PQ at  $Q_n$  (31).

The positions of the two non-redox-active groups are also consistent with previous structures, showing that 9-*cis*- $\beta$ -carotene ( $\beta car$ ) protrudes toward the membrane inserted between PetM and PetG (Fig. 3G), while the ring of chlorophyll  $a$  (Chl  $a$ ) interacts with two helices of SubIV (Fig. 3H). However, the phytol tail of Chl  $a$ , which, in our structures, protrudes toward the intermembrane cavity (IC) between the monomers, can adopt different orientations in various structures (18–20). In addition to the previously described subunits of Cyt  $b_6f$ , we detected an additional peptide density bound within a groove on the stromal side of both monomers, formed between Cyt  $b_6$ , SubIV, PetG, PetM, and PetN (Fig. 3I). As none of the sequences of known Cyt  $b_6f$  components fitted the very well-resolved map, we used mass spectrometry (MS) to identify major copurifying proteins. We found several peptides of the thylakoid soluble phosphoprotein (TSP9) protein (fig. S4A). A stretch of 25 amino acids of its conserved region can be modeled unambiguously into the orphan densities in both monomers (Fig. 3I and fig. S4, B and C). TSP9 is known to contain a short helical motif (32), which, in Cyt  $b_6f$ , positions several hydrophobic residues in proximity of the  $\beta car$  molecules. A second short helix is

formed upon binding to Cyt  $b_6f$  at the opposite end of the bound stretch, but the remaining C-terminal half of TSP9 remains unstructured.

### Endogenous PQs form a channel in Cyt $b_6f$

Notably, six native PQ molecules (three in each monomer, denoted PQ1–PQ3) were detected close to the p-side of Cyt  $b_6f$  (Fig. 4A and fig. S5). In both monomers, three PQ molecules line up one after another, resulting in a tail-head-tail-head-tail-head arrangement (from right to left in Fig. 4A). The coordination of all PQs is highly unanticipated, given that other occupants of  $Q_p$  were typically reported to bind in the opposite orientation (18, 33, 34). This continuous assembly discloses the presence of a PQ channel (one in each monomer) that starts at one side of Cyt  $b_6f$  (Fig. 4B), passes through  $Q_p$  to IC (Fig. 4C), and lastly reaches the outlet at the other side of the monomer (Fig. 4D). In detail, the tail of PQ1 is bound in a cavity formed between helices of PetG and SubIV through a number of specific interactions and even contacts the Chl  $a$  ring (Fig. 4B). The head group of PQ1 is positioned very close to 2Fe2S, and the first three isoprenoid moieties after the head group are rather flexible, located close to the border of the lipid membrane, and curved toward the inside of the protein. It appears that PQ1 cannot proceed into the  $Q_p$  reaction cavity because the ISP partially blocks the entry site. In addition, the last two isoprene moieties of the tail of PQ2 already occupy the part of the channel spanning from  $Q_p$  to IC. We find two possible conformations of the head group of PQ2, which either protrudes straight into the IC or wraps around the phytol chain of Chl  $a$  (Fig. 4C). The tail of PQ3 is arched around the transmembrane helix of the ISP and

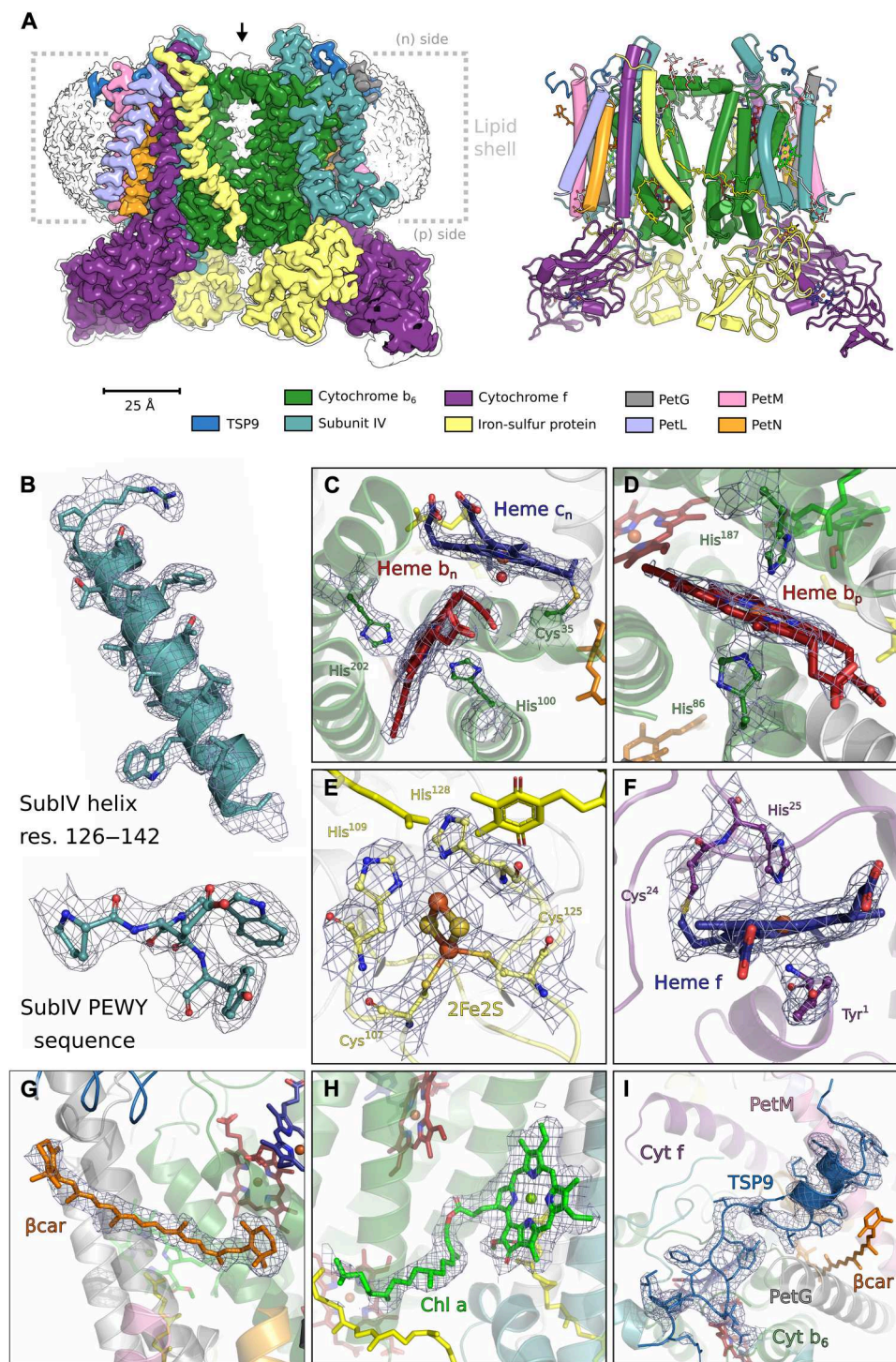


**Fig. 3. Overview of the structure and close-up views of the selected structural elements and prosthetic groups of Cyt  $b_6/f$ .** (A) Cryo-EM density map (left) and a model of the Cyt  $b_6/f$  structure (PDB: 7ZYV). (B) Fragments of SubIV: helix (top) and PEWY motif (bottom). (C to F) The structures of the redox-active prosthetic groups (sticks) with the respective ligands of the metal ions (balls and sticks): (C) the pair of hemes  $b_n$  and  $c_n$ , (D) heme  $b_p$ , (E) the 2Fe2S cluster, and (F), heme f. (G to I) The non-redox-active groups: (G)  $\beta$ -carotene, (H) Chl a, and (I) fragment of TSP9 bound to Cyt  $b_6/f$ . The grids show the density maps around the atoms of the groups, while ribbons in (B) to (I) show surroundings of the prosthetic groups. Yellow sticks show PQ molecules.

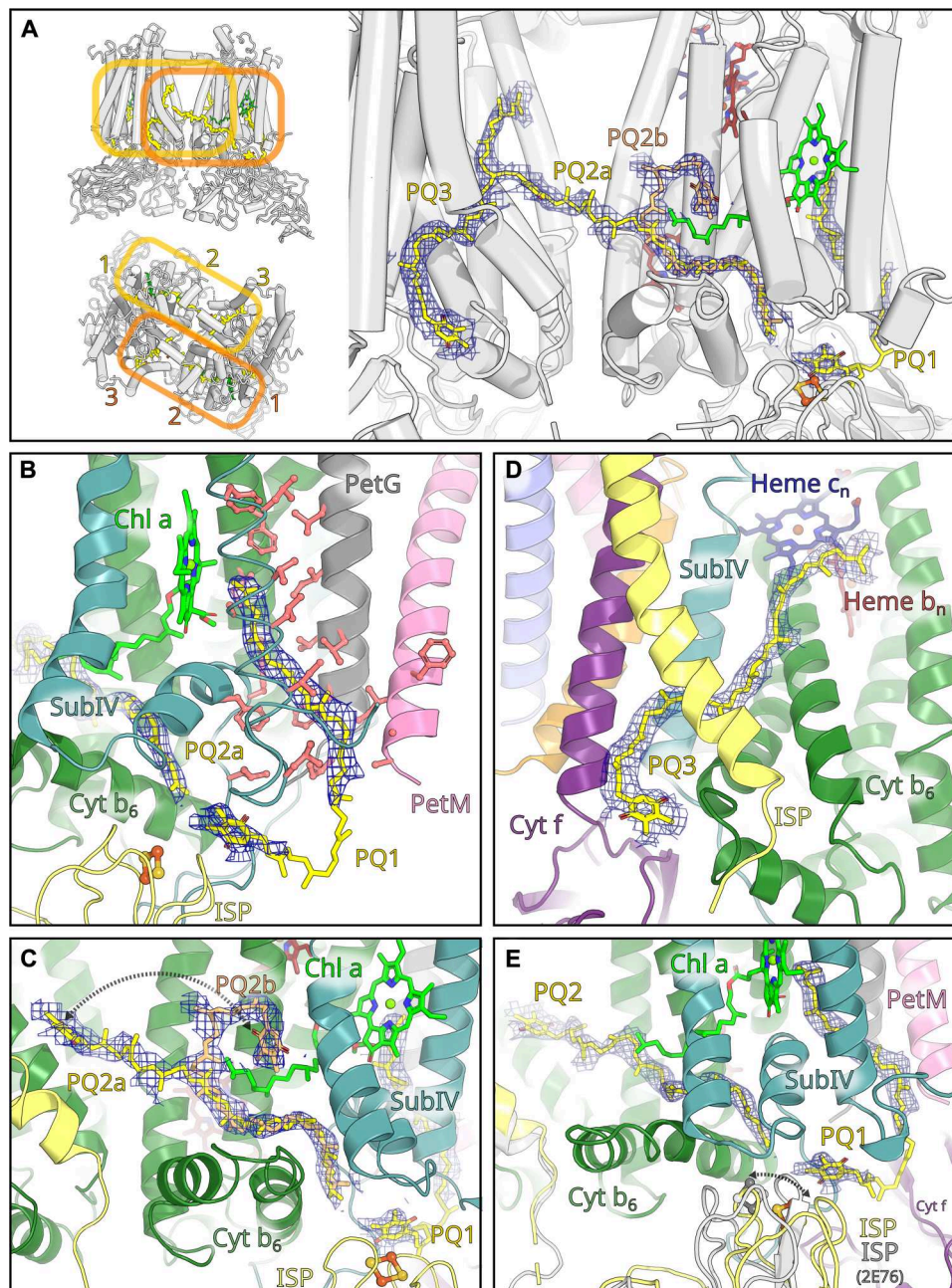


**Fig. 4. Structure of PQ molecules in Cyt  $b_6f$ .** (A) At the p-side of Cyt  $b_6f$ , three PQ molecules are similarly located in each monomer as indicated by yellow and orange frames in two perpendicular projections (left) and in a close-up view of one monomer (right). (B) PQ1 at the entry point. (C) PQ2 protruding to the intermonomer cavity. (D) PQ3 at the exit point. (E) PQ1 and PQ2 occupying the  $Q_p$  cavity. Yellow and orange balls and sticks show the position of 2Fe2S interacting with PQ1, while gray shows the position of the cluster overlaid from the crystal structure of Cyt  $b_6f$  (PDB: 2E76) with bound TDS [tridecylstigmatellin; TDS is not displayed in (E) for clarity; see fig. S7 for the structure with TDS]. The two respective positions of ISP-HD are also shown in yellow and gray. The proposed motion of 2Fe2S to the catalytically active position is marked by dotted gray arrow. Numbers 1 to 3 in (A) denote the position of PQ1 to PQ3, respectively. PQ2a and PQ2b show two possible orientations of PQ2 molecule.

shows considerable flexibility, while the head of PQ3 is well defined and exits between the transmembrane helices of ISP and of Cyt  $f$  in the second monomer (Fig. 4D). The end of the PQ3 tail can occupy similar positions as the head group of PQ2 and might block PQ2 from leaving IC and  $Q_p$ . Notably, the densities for PQ1, PQ2, and PQ3 are less well resolved but also clearly visible in the Cyt  $b_6f$ -PC complex at 2.7 Å resolution (fig. S5, B and C). In addition, we used

symmetry expansion and masked three-dimensional (3D) variability analyses to circumvent averaging effects and enhance the local positions of quinone molecules (fig. S5D). Hence, we observed consistent PQ densities using different preparation protocols and separate symmetric and asymmetric density reconstruction procedures.

In addition to the six PQ molecules resolved symmetrically in both monomers in our structures, one additional PQ molecule has already been described in the previous Cyt  $b_6f$  cryo-EM structure. The head of this PQ occupies  $Q_n$  (we thus name it  $PQ_n$ ), while its isoprenoid tail is arched, with the end fragment reaching  $Q_n$  in the other monomer.  $PQ_n$  has been discussed in the context of possible transitions between  $Q_p$  and  $Q_n$  in opposite monomers during the catalytic cycle (20).

### Model of one-way diffusion of quinones

The unexpected positioning of  $PQ_1$ – $PQ_3$  prompted us to develop a model for the one-way diffusion of quinones through the channel during the catalytic cycle (Fig. 5A). The model proposes that  $PQ_1$  and  $PQ_3$  occupy the possible entry and exit points, respectively, while  $PQ_2$  represents the position of quinone in the middle of the channel. The initial binding of the PQ tail can occur through the helices of PetG and SubIV and, therefore, without leaving the hydrophobic environment of the membrane. However, the binding in the Chl a cavity would impose a strain onto the PQ molecule by forcing the isoprenoid moieties to come closer to the hydrophilic

part of the membrane. This spatial arrangement makes the tail of  $PQ_1$  flip the head group toward the channel entrance and His<sup>128</sup> of the ISP, which coordinates  $2Fe_2S$ . In our model, the head group of  $PQ_1$  could remain highly dynamic until it engages with the  $2Fe_2S$ , potentially explaining its rather weak density profile. Once  $PQ_1$  enters the channel, it would proceed to the next position defined by  $PQ_2$ , which passes the phytol chain of Chl a at IC (Fig. 4C). The  $PQ_2$  molecule can diffuse through IC toward  $Q_n$ , where it occupies a position analogous to previously described  $PQ_n$  and then exit with its head oriented to the stromal side of the lipid bilayer or move back to  $Q_p$  as part of CET according to the mechanism proposed by (12, 15). Alternatively, as our structure suggests,  $PQ_2$  can exit through the route defined by the position of  $PQ_3$  (Fig. 4D). Thereby, it would reach the membrane bilayer with its head group facing the lumen, like it started. Thus, the initial binding involves just a slip of the PQ tail into the protein cavity, while, upon exiting, PQ is already predisposed to readopt its natural orientation in the membrane. This second route seems to be more probable when the  $Q_n$  site is already occupied by a  $PQ_n$  molecule in the configuration presented in the previous higher plant structure of Cyt  $b_6f$

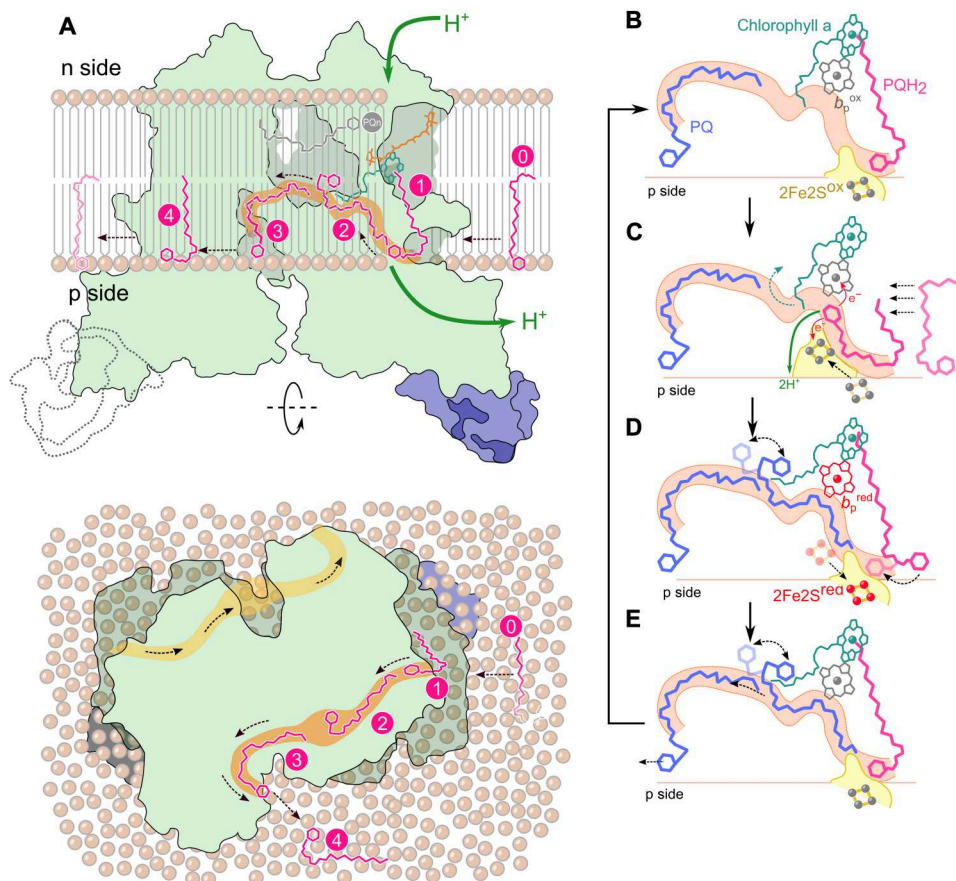


**Fig. 5. Model of one-way diffusion of quinones through the channels in Cyt  $b_6f$ .** (A) Schematic view of Cyt  $b_6f$  (green) with bound PC (blue) in orientation parallel or perpendicular to the membrane plane (top and bottom, respectively) showing the consecutive positions of quinones during their diffusion. Numbers in magenta circles (0 to 4) denote the static positions of quinones while diffusing from and to the membrane through the channel (orange tube) in one monomer. The numbers 1, 2, and 3 correspond to  $PQ_1$ ,  $PQ_2$ , and  $PQ_3$  observed in our structure, respectively. The channel in the second monomer is shown in yellow. (B to E), Proposed sequence of events leading to the oxidation of  $PQH_2$  (magenta sticks) to generate PQ (blue sticks) at  $Q_p$ . Direction of PQ diffusion and motion of  $2Fe_2S$  are shown as dotted black arrows, while proton translocation and electron transfer are shown as green and red solid arrows, respectively. Dotted green arrow indicates motion of phytol chain of Chl a to open the channel for quinones. Gray and red cofactors (hemes and  $2Fe_2S$ ) denote oxidized and reduced states, respectively.

(20). We note that the proposed PQ diffusion between  $Q_p$  and  $Q_n$  thorough the IC does not preclude binding of  $PQ_n$  to  $Q_n$  directly from the membranous pool of PQs (fig. S6).

Even without applying symmetry during any step of the reconstruction, the two channels on both sides of the dimer are nearly identically occupied by PQ1, PQ2, and PQ3, indicating that both channels equally contribute to the quinone traffic (Fig 4A and fig. S5). At the same time, according to the model inferred from the structure of plant Cyt  $b_6f$  (20), only one  $PQ_n$  can bind to one of the two  $Q_n$  sites is such a configuration where its head occupies  $Q_n$  in one monomer, while its tail blocks entrance to  $Q_n$  of the second monomer. We do observe a residual density at a similar position proposed for  $PQ_n$ , but the location on the symmetry axis of the respective density for this molecule might be biased by symmetry and pseudo-symmetry. Therefore, our reconstructions cannot prove or disprove the presence of a  $PQ_n$  molecule that spans between the two monomers. On the other hand, PC is bound only to one monomer, suggesting that the interaction of Cyt  $b_6f$  with PC and diffusion of quinones through the channels are mechanistically uncoupled and happen independently.

### Transient catalytic configuration of plastoquinol at $Q_p$

It is generally assumed that the position of the chromone ring of the Cyt  $b_6f$  inhibitor tridecylstigmatellin (TDS), which occupies  $Q_p$ , approximates the position of  $PQH_2$  in the conformation predisposed for the BR (34). In this scenario, the ISP mobile head domain (ISP-HD) approaches  $Q_p$  (PDB: 2E76; Fig. 4E) placing the ring of TDS less than 14 Å away from both 2Fe2S and heme  $b_p$ , which is required for competent electron transfer (fig. S7) (30). While we find the density for the head group of PQ1 in close proximity to the 2Fe2S (~6.5 Å from ISP:His<sup>128</sup>), it is ~23 Å away from the edge of heme  $b_p$ . Furthermore, ISP-HD is shifted ~6.5 Å away from  $Q_p$  (Fig. 4E). Therefore, PQ1 and ISP are not found in a conformation that can be considered optimal for BR, neither are the head groups of the remaining PQ2 and PQ3 molecules. Thus, we propose that the catalytically active configuration is highly transient and that BR occurs, while PQ is transitioning through the channel between the PQ1 and PQ2 positions [see model in Fig. 5 (B to E)]. In detail,  $PQH_2$  binds to the Chl a cavity of Cyt  $b_6f$  and positions its head group for entering the channel (Fig. 5B). Once the channel is accessible,  $PQH_2$ , together with ISP-HD, diffuses into the channel to transiently reach the position competent for BR (Fig. 5C). Immediately after the reaction, PQ moves further along the channel to reach the PQ2 position. The movement displaces the phytyl tail of Chl a, which occupies the channel (as seen in PDB: 6RQF) and prevents other PQs from the IC side from slipping back toward  $Q_p$ . The head of PQ wraps around the phytyl chain of Chl a and allows the ISP-HD to move back to accept the next incoming  $PQH_2$  molecule at the entry site (Fig. 5D). Next, PQ moves to the position defined by PQ3, from which it can diffuse back to the membrane (Fig. 5E). In this model, different conformations of the tail of Chl a affect the traffic of PQ through the channel, which translates into a putative regulatory role of Chl a. This hypothesis would be in line with a previously proposed gating function of Chl a at  $Q_p$  (33).

### Mechanistic consequences of quinone traffic through Cyt $b_6f$

Our model creates an unprecedented conceptual framework for understanding the molecular processes happening throughout the

catalytic BR at  $Q_p$ . It also simplifies the mechanistic description of the dynamics of quinones necessary to pass through all intermediate steps. It proposes that diffusion of quinones occurs in one direction through a channel, which has shallow potential wells that correspond to positions of PQ1, PQ2, and PQ3 on the way from the entry to the exit point. It replaces a rather convoluted classical model, which stated that  $PQH_2$  enters headfirst from the IC and after the BR the product leaves the catalytic site retracting through the same channel in opposite direction. That model considered the orientation of TDS found at  $Q_p$  in several structures of Cyt  $b_6f$  as mimicking binding of PQ, thus the channel was presumed to face the IC side. This seemed unquestionable, as most of the other inhibitors of  $Q_p$ , including those of Cyt  $bc_1$ , also bind in a similar orientation (35–37). We find an inverted head-to-tail orientation of endogenous PQ, which places the isoprene moieties of the tail deeply buried in the channel; incidentally, this recapitulates the seemingly unusual orientation of TDS found in one of the earliest Cyt  $b_6f$  structures (PDB: 1VF5; fig. S7) (19, 38). This indicates that TDS and other  $Q_p$  inhibitors typically bind in opposite orientation than PQ1–PQ3, which perhaps contributes to their efficient inhibition.

In our model, the entrance for quinones occurs at a site never considered before. Nonetheless, 2,5-dibromo-3-methyl-6-isopropylbenzoquinone (DBMIB), a potent inhibitor of  $Q_p$  that forms a stable semiquinone-2Fe2S state (39), was found in the crystal structure bound in the region of PQ1 (fig. S7) (40). It was thus hypothesized that DBMIB, which is of similar size and structure as the PQ head group, enters the catalytic  $Q_p$  cavity from the channel entry side (40). We propose that quinones will also find enough space to reach  $Q_p$  from this side, provided that ISP-HD moves along with the quinone ring from the position defined by PQ1. Furthermore,  $\beta$ car, inserted between the helices of PetM and PetG, which seem to be involved in binding of PQ1 by providing interactions between residues 1 to 6 and 6 to 11 of PetM and PetG, respectively, with the isoprenoid tail, might influence the spatial arrangement of these helices upon a cis-to-all-trans transition of  $\beta$ car. It is tempting to speculate that such an isomerization, in analogy to previously observed isomerization for other carotenoids (41, 42), could change the affinity of the incoming quinone molecule and therefore influence the supply of substrates for  $Q_p$ .

Furthermore, we identified TSP9 as a binding partner for Cyt  $b_6f$ , which is in direct contact with  $\beta$ car. It was shown that TSP9 undergoes phosphorylation upon exposure of chloroplasts to light and also interacts with the light-harvesting complex II, PSI, and PSII, playing a possible role in photosynthetic state transitions (43). It remains to be examined whether interaction of TSP9 with Cyt  $b_6f$  also plays a role in this process. There is yet another possible function for TSP9, which comes from the observation that it binds in the region where a potential n-side electron donor protein is considered to bind to Cyt  $b_6f$  to support CET (2, 44). It is tempting to speculate that TSP9 and such a protein compete for binding to Cyt  $b_6f$ , in which case, TSP9 would play a specific role in regulating the ratio between LET and CET in higher plants. A similar concept, although involving different regulatory protein, has recently emerged for cyanobacterial Cyt  $b_6f$ . The cryo-EM structure of this complex revealed a subunit PetP bound (45) in a similar region where TSP9 binds to plant Cyt  $b_6f$ . PetP is an auxiliary subunit specific only to cyanobacterial Cyt  $b_6f$  and is already shown to regulate the balance

between CET and LET (46). Thus, PetP and TSP9 might play the same regulatory role in cyanobacteria and plants, respectively.

It remains to be shown experimentally whether  $\beta$ car, TSP9, and Chl a are involved in regulation of the coordinated movement of quinones through the channel in a biologically relevant manner, possibly linked with changes in light exposure. Nevertheless, it can be hypothesized that any regulation of this movement will affect the rate of reaction at  $Q_p$  and subsequent electron delivery to  $Q_n$ .

Given the high structural and functional similarities between Cyt  $b_6f$  and Cyt  $bc_1$ , a question arises whether a simple one-way traffic of quinones should be considered only for Cyt  $b_6f$  or rather as a more universal concept for all Cyt  $bc$  family members. On the mechanistic side, the proposed concept does not preclude reversibility of catalytic reactions, which is well characterized for Cyt  $bc_1$  (11, 47). The traffic may be blind to the redox state of quinones, and the respective catalytic reaction would proceed on the basis of the appropriate redox states of  $2Fe_2S$  and heme  $b_p$  when the substrate reaches  $Q_p$ , i.e., oxidation of quinol would take place when both cofactors are oxidized, while the reduction of quinone would happen when both cofactors are reduced. On the structural side, a quick inspection of the structure of bacterial Cyt  $bc_1$  allows for identification of a similar potential quinone channel. However, Cyt  $bc_1$  does not have Chl a nor  $\beta$ car, which emerge as possible structural elements functionally associated with the channel of Cyt  $b_6f$ . In addition, these two complexes respond differently to the specific quinonoid inhibitors of the catalytic site. We thus do not dismiss the possibility that the proposed traffic through the channel is a unique feature of Cyt  $b_6f$ .

While our structure-based model introduces a different description for quinone traffic through Cyt  $b_6f$ , it is still consistent with overall mechanistic concept behind BR. Unprecedented is the proposal that quinones continuously pass through the channel, predominantly filling the catalytic site with the redox-inactive isoprenoid chain and only transiently exposing the redox-active ring for the catalytic reaction. This proposal clearly needs to be tested in further studies; nevertheless, it provides the attractive conceptual framework to be considered when addressing the flow of quinones in photosynthesis and respiration.

## MATERIALS AND METHODS

### Materials

Buffers, salts, and decylplastoquinone were purchased from Sigma-Aldrich. Detergents undecyl  $\alpha$ -D-maltoside (UDM) and octyl glucoside (OG) were purchased from Glycon (Germany). Propyl-Sepharose resin was prepared using activated Sepharose-CNBr powder purchased from Cytiva (Sweden). The activated Sepharose-CNBr was reacted with propylamine (Sigma-Aldrich) according to the manual delivered by the supplier.

### Isolation of Cyt $b_6f$

#### Protocol 1

Protocol 1 was used to isolate Cyt  $b_6f$  that was subsequently used to obtain the structure of Cyt  $b_6f$  with plastocyanin bound (PDB: 7QRM). Dimeric Cyt  $b_6f$  was isolated from market spinach (*Spinacia oleracea*) leaves using a large-scale protocol adapted from Baniulis *et al.* and Romanowska (48, 49). The leaves were homogenized using a whole slow juicer in buffer 1 [50 mM tris (pH 8), 50 mM

NaCl, 200 mM sucrose, and antifoam A (0.2 ml/liter)]. The obtained solution was filtered through a sieve and a must filter before centrifugation at 17,000g for 20 min, 4°C. The pellet containing chloroplasts was suspended in buffer 2 [10 mM tris (pH 7.5) and 10 mM NaCl] and passed through a 50- $\mu$ m filter. After the addition of protease inhibitors [benzamide,  $\epsilon$ -aminocaproic acid, and phenylmethylsulfonyl fluoride (PMSF)], the chloroplast suspension was passed through a French press (16,000 psi), followed by centrifugation at 1000g for 5 min at 4°C. The collected supernatant was ultracentrifuged at 148,000g for 30 min at 4°C. The pellet containing thylakoid membranes was used for the subsequent Cyt  $b_6f$  purification steps, while the supernatant was stored for isolation of PC (see the "Isolation of PC" section). The pellet was resuspended in buffer 3 [30 mM tris (pH 7.5), 50 mM NaCl, and 1 mM EDTA], and the chlorophyll content was determined using the protocol described by Porra *et al.* (50). The solution was adjusted to a concentration of 1.5 mg/ml of chlorophyll by dilution with buffer 3. An equal volume of buffer 4 [buffer 3 supplemented with 52 mM OG, 0.2% sodium cholate, and 400 mM ammonium sulfate (AS)] was slowly added to achieve selective solubilization of thylakoid membranes. The solution was stirred for 15 min and ultracentrifuged at 148,000g for 20 min at 4°C. The supernatant was brought to 37% of AS saturation and centrifuged at 24,000g for 10 min at 4°C and then filtered through a 220-nm membrane before loading onto a propyl-Sepharose column preequilibrated with buffer 5 (buffer 3 with 1 mM UDM and 37% of AS saturation). The column was washed thoroughly with buffer 5 until the eluent was colorless, and then, a greenish brown band containing Cyt  $b_6f$  was eluted with buffer 6 (buffer 3 with 1 mM UDM and 20% of AS saturation). The eluent was brought to 37% of AS saturation and centrifuged at 24,000g for 10 min at 4°C. The supernatant was filtered through 220-nm membrane and loaded onto a second propyl-Sepharose column preequilibrated with buffer 5. The column was washed stepwise with buffer 5 containing decreasing amounts of AS (saturation decreasing from 35 to 30%), before a brownish band was eluted with buffer 6. The eluate was concentrated using microconcentrators (Merck Millipore), and the buffer was exchanged to buffer 7 (buffer 3 with 1 mM UDM). The sample was loaded onto a 10 to 25% continuous sucrose gradient in buffer 7 and ultracentrifuged at 141,000g for 16 hours, 4°C. A brown band in the middle of the gradient containing pure Cyt  $b_6f$  was carefully collected, and the buffer was exchanged to buffer 7. Further biochemical analysis [including enzymatic activity, optical and electron paramagnetic resonance (EPR) spectroscopy, and electrophoretic analysis] indicated that this fraction contained a full complement of the Cyt  $b_6f$  subunits (fig. S1, A to C) and was enzymatically active (see the "Activity measurements" section below). Therefore, this fraction was used for cryo-EM.

#### Protocol 2

Protocol 2 is a modified protocol 1 designed to limit the number of steps and chemical compounds used in purification. The major modifications included (i) the replacement of a French press for chloroplast disruption with a combination of sonication and freeze-thawing, (ii) the usage of only one detergent for solubilization of thylakoid membranes (UDM), (iii) the optimization for hydrophobic interaction chromatography steps, and (iv) the omission of the sucrose gradient centrifugation. The Cyt  $b_6f$  structure (PDB: 7ZYV) was determined from the sample purified following protocol 2. In detail, chloroplasts, obtained as described in the protocol 1,

were suspended in buffer 2 and stored frozen at  $-80^{\circ}\text{C}$ . A batch of around 100 ml of chloroplast suspension was thawed. After the addition of protease inhibitors (benzamidine,  $\epsilon$ -aminocaproic acid, and PMSF; final concentration of 1 mM each), the chloroplast suspension was kept in an ice-water bath for cooling, and it underwent sonication using a 500-W ultrasonic processor (VCX 500) with 13-mm tip. Ultrasonic pulse sequence parameters were as follows: 100% power; pulse length, 30 s; pulse interval, 60 s; and total pulse time, 8 min. Afterward, the suspension was ultracentrifuged at 148,000g for 20 min at  $4^{\circ}\text{C}$ , and the pellet of thylakoid membranes was collected, resuspended in buffer 3, and frozen overnight. After thawing, the thylakoid suspension was homogenized using a glass homogenizer. The total chlorophyll content was determined as described in protocol 1. Further steps were performed under dim green light conditions. The solution was diluted with buffer 3 to obtain the final concentration of chlorophyll (3.0 mg/ml). An equal volume of buffer 3 with UDM (12 mg/ml) was added to solubilize thylakoid membranes (UDM:chlorophyll mass ratio was 4:1). The solution was stirred for 15 min and ultracentrifuged at 148,000g for 20 min ( $4^{\circ}\text{C}$ ) twice to remove unsolubilized material. Solid AS was added to the supernatant (37% saturation). The solution was stirred for 10 min and centrifuged twice at 24,000g (25 min at  $4^{\circ}\text{C}$ ) and then filtered through a 0.22- $\mu\text{m}$  syringe filter. Because of the positive temperature coefficient of hydrophobic interactions, the chromatography on propyl-Sepharose column was performed at room temperature.

The sample was loaded onto the column (column internal diameter, 54 mm; bed volume,  $\sim 80$  ml) preequilibrated with buffer 5. The column was washed thoroughly [at least 5 column volumes (CVs)] with buffer 5. Buffer 6 was used for elution, and the eluent was collected in fractions. Each fraction was analyzed in an ultraviolet-visible spectrometer (dithionate reduced–ferricyanide oxidized differential spectrum), and only those containing Cyt  $b_6f$  were pooled and concentrated on Amicon Ultra 50 kDa to the final volume of  $\sim 10$  ml. Solid AS was added to raise the percent of AS saturation from 20 to 37% in the sample. The sample was stirred, centrifuged at 24,000g for 20 min at  $4^{\circ}\text{C}$ , and filtered through a 0.22- $\mu\text{m}$  syringe filter. The sample was loaded onto a second propyl-Sepharose column (column internal diameter, 15 mm; bed volume,  $\sim 12$  ml) preequilibrated with buffer 5. Washing was done as follows: 1 CV of buffer 5 and 5 CV of buffer 3 with 30% AS saturation and 1 mM UDM. Note that during this step, a brownish band and a green band should begin to separate from each other. Elution of brownish Cyt  $b_6f$  band was performed with buffer 3 with 25% AS saturation and 1 mM UDM (green band containing mostly PSI stays on column). The sample containing Cyt  $b_6f$  was concentrated and desalted.

Because the sucrose gradient fractionation was omitted, the sample contained a mixture of monomers and dimers of Cyt  $b_6f$ , which was taken into account during the initial cryo-EM particle classification. In addition, the sample contained FNR (ferredoxin–reduced form of nicotinamide adenine dinucleotide reductase), as seen in SDS–polyacrylamide gel electrophoresis (SDS–PAGE) (fig. S1D) and MS analysis (fig. S5A). We found that it is a result of a similar affinity of both FNR and Cyt  $b_6f$  to the propyl-Sepharose resin, i.e., both proteins can bind to and elute from the column under the similar conditions. The copurification of Cyt  $b_6f$  and FNR has been described in literature (51). The concentration of Cyt  $b_6f$  isolated using both protocols was assessed spectrophotometrically by measurement of ascorbate-reduced minus

ferricyanide-oxidized absorption spectra at 554 nm, relative to isobestic point 543 nm, and using hem *f* differential extinction coefficient  $\epsilon_{554-543} \approx 25 \text{ mM}^{-1} \text{ cm}^{-1}$ .

### Isolation of PC

Supernatant collected after ultracentrifugation of thylakoid membranes (see the “Isolation of Cyt  $b_6f$ ” section) was salted out with 65% AS. The precipitate was separated from the liquid phase by centrifugation for 25 min at 24,000g and  $4^{\circ}\text{C}$ . Crystalline potassium ferricyanide was added to the resulting supernatant to a concentration of 1 mM. Then, the supernatant was loaded on a Sepharose 4B column equilibrated with 10 mM tris (pH 7.5), 0.1 mM EDTA, and 1 mM potassium ferricyanide (buffer 8) at 65% AS saturation. The column containing bound PC was washed with the same buffer (buffer 8 + 65% AS saturation), and then, PC was eluted from the column with buffer 8 at 20% AS saturation. The PC-containing eluent was concentrated and desalted on centrifugal filter units and then loaded on a DEAE Sepharose Fast Flow column equilibrated with buffer 8. Under these conditions, PC only weakly bound to the resin and slowly flowed through it. The PC-containing fractions were pooled, and solid AS was added to a concentration of 60%. After centrifugation for 25 min at 24,000g and  $4^{\circ}\text{C}$ , the sample was loaded on Toyopearl Ether-650M column equilibrated with buffer 8 at 60% AS. The column with bound PC was washed with two volumes of buffer 8 at 50% AS, and then, PC was eluted with buffer 8 at 40% AS. The eluted PC was then desalted and concentrated to 2.6 mM. The extinction coefficient used to calculate concentration of PC was  $\epsilon_{597} = 4.9 \text{ mM}^{-1} \text{ cm}^{-1}$  (52).

### Optical and EPR spectroscopy

Absorbance spectra of the isolated Cyt  $b_6f$  complexes were measured at room temperature using a Biologic Diode Array spectrophotometer. Cyt  $b_6f$  was oxidized by addition of potassium ferricyanide. Fully reduced samples were obtained by the addition of a small grain of solid sodium dithionite. Continuous-wave EPR spectra were recorded at 10 K on a Bruker ElexSys E580 spectrometer equipped with SHQE0511 resonator and a set for liquid helium measurements consisting of ESR900 cryostat and ITC503S temperature controller (Oxford Instruments). Oxidized and partially reduced samples were obtained by the addition of small aliquots of potassium ferricyanide and a small grain of sodium ascorbate, respectively, to the EPR tube. Measurement parameters were as follows: microwave frequency, 9.39 GHz; microwave power, 6.35 mW; modulation amplitude, 1.5 mT at 100 kHz; conversion time, 163.8 ms; and sweep time and width, 671 s and 450 mT.

### Activity measurements

The activity of Cyt  $b_6f$  was determined by measuring the Cyt  $b_6f$ -mediated reduction of PC. Before the activity measurements, substrates for Cyt  $b_6f$  were prepared in the following way. PC was oxidized with potassium ferricyanide, which was later removed by concentration-dilution cycle on microconcentrators (10-kDa cutoff). Decylplastoquinone was dissolved in ethanol and reduced to decylplastoquinol (dPQH<sub>2</sub>) with hydrogen gas in the presence of platinum on carbon as the catalyst. After reduction, dPHQ<sub>2</sub> was diluted three times with dimethyl sulfoxide.

The enzymatic reaction was carried out in 30 mM tris (pH 7.5), 50 mM NaCl, 1 mM EDTA, and 1 mM UDM, containing 20  $\mu\text{M}$  oxidized PC and 100  $\mu\text{M}$  dPQH<sub>2</sub>. The total volume of the reaction

mixture was 1 ml. The reaction was initiated by injection of Cyt  $b_6f$  to a final concentration of 20 nM (referring to the concentration of Cyt  $f$ ), and the reaction progress was monitored using a Biologic Diode Array spectrophotometer. The PC reduction rate was determined from the initial slope after the addition of Cyt  $b_6f$  to the cuvette. With this method, the turnover rate of the fraction used for cryo-EM analysis was estimated to be approximately 120 per second.

### Preparation of cryo-EM samples

Before the preparation of the cryo-EM sample of Cyt  $b_6f$  with PC (protocol 1), the purified proteins were transferred to the buffer containing 10 mM tris (pH 7.5), 15 mM NaCl, and 0.7 mM UDM. Subsequently, Cyt  $b_6f$  was mixed with PC to reach a final concentration of 38.7 and 100  $\mu$ M (referring to Cyt  $f$  concentration), respectively. Shortly before freezing the sample, OG was added to a final concentration of 1.17% (m/v, 2.6 mM). For preparation of the cryo-EM sample of Cyt  $b_6f$  without PC (protocol 2), purified Cyt  $b_6f$  was transferred to the buffer containing 10 mM tris (pH 8.0), 15 mM NaCl, and 0.8 mM UDM and concentrated to 56  $\mu$ M (referring to Cyt  $f$  concentration). For both samples, vitrification procedure was the identical: Three microliters of the respective sample was applied onto freshly glow-discharged transmission electron microscopy grids (Quantifoil R2/1, Cu 200 mesh) and plunge-frozen into liquid ethane by a Vitrobot Mark IV (Thermo Fisher Scientific). The following parameters were used: 100% humidity, 277 K, 2-s blot time, 0-s wait time, blot force of  $-1$ , 0-s drain time, and total blot of 1. Frozen grids were kept in liquid nitrogen until further use.

### Data acquisition and processing

Cryo-EM data were collected at the National Cryo-EM Centre SOLARIS (Kraków, Poland). Datasets containing 7784 and 7651 movies (40 frames each) for Cyt  $b_6f$ -PC and Cyt  $b_6f$ , respectively, were collected with a Titan Krios G3i microscope (Thermo Fisher Scientific) at 300 kV accelerating voltage, magnification of 105,000, and corresponding pixel size of 0.86 Å/pixel (fig. S2A). A K3 direct electron detector was used for data collection in a BioQuantum Imaging Filter (Gatan) setup with 20-eV slit width. The K3 detector was operated in counting mode. Imaged areas were exposed to 40  $e^-/\text{Å}^2$  total dose (corresponding to a dose rate of  $\sim 16 e^-/\text{pixel}$  per second measured in vacuum). The images were acquired under focus optical conditions with a defocus range of  $-2.1$  to  $-0.9 \mu\text{m}$  and with 0.3- $\mu\text{m}$  steps. Cyt  $b_6f$ -PC dataset was analyzed first with cryoSPARC v3.3.1 (53–56), where "patch motion correction" and "patch contrast transfer function (CTF) estimation" were performed. Next, blob picker was used for preliminary particle picking. Acquired sets of particles were subsequently 2D classified and used in the generation of preliminary classes for template picking. The application of a template picker and 2D classification resulted in a set of 177,412 particles (fig. S2B). This set was used in a heterogeneous refinement for cleaning purposes and particles from the better-resolved class served as an input for another heterogeneous refinement dividing particles of Cyt  $b_6f$  into two classes. The particle set was globally and locally CTF-refined and passed to a final "non-uniform (NU) refinement" resulting in a density map with 2.7 Å overall resolution (fig. S2C) and a much higher local resolution of central parts of the map (fig. S2E). Unfortunately, the density for PC was still hard to unambiguously interpret. Therefore, 97,597 particles used for the last refinement were exported to

RELION v3.1.2 (57) for further 3D classification. From three classes, the best one was used in masked 3D auto refinement with very low orientational bias (fig. S2F). Postprocessing of the refined volume resulted in a density map with an overall resolution of 3.18 Å and an improved density for the regions containing PC (fig. S2D). Cyt  $b_6f$  dataset was analyzed in cryoSPARC v3.3.1. After performing patch motion correction and patch CTF estimation, a blob picker was used to generate templates for template picking. At total of 435,204 Cyt  $b_6f$  particles from the heterogeneous refinement were used for TOPAZ training and subsequent TOPAZ picking (58, 59), and 579,877 curated TOPAZ picked particles were combined with 435,204 template picked particles, followed by duplicate particles removal. After one 2D classification and one ab initio curation step, the remaining 685,979 particles were local motion-corrected and used in a nonuniform refinement with iterative CTF refinement to solve the final 2.13 Å resolution structure (fig. S2, B to D). Local resolution estimation shows uniform high resolution of Cyt  $b_6f$  (fig. S2E), resulting from very low orientational bias (fig. S2F) as exemplified by 2D class averages (fig. S2G). The atomic models were built using Coot (60), refined using Phenix (61), and validated using MolProbity (62).

### Peptide identification by MS

Peptide samples were prepared in three replicates. Proteins from sample containing the studied complex were precipitated by the addition of trichloroacetic acid to a final concentration of 30%. After 2 hours of incubation at 4°C, samples were centrifuged (17,000g, 10 min, and 4°C). Supernatants were collected and loaded onto C18 StageTips for peptide purification (63). The peptides of one replicate were additionally cleaned up with the use of paramagnetic beads (64). The resulting samples were analyzed by nano liquid chromatography–tandem MS (LC-MS/MS) on a Q-Exactive mass spectrometer coupled to an UltiMate 3000 RSLCnano system (Thermo Fisher Scientific). The peptides were separated with a 30-min gradient of 2 to 40% acetonitrile with 0.05% formic acid and analyzed by mass spectrometer using the Top3 method. MS and MS/MS spectra were acquired at resolutions of 70,000 and 35,000, respectively. The dynamic exclusion option was disabled. The RAW files were processed with the Proteome Discoverer platform (v.1.4, Thermo Fisher Scientific) and searched against the UniProtKB *S. oleracea* reference proteome (accessed in April 2022; 23,484 sequences) using the locally installed MASCOT search engine (v.2.5.1, Matrix Science). The following parameters were applied: enzyme, none; variable modification, methionine oxidation; peptide mass tolerance, 10 parts per million; and fragment mass tolerance, 20 milli mass unit (mmu).

### Supplementary Materials

This PDF file includes:

Figs. S1 to S7

Table S1

[View/request a protocol for this paper from Bio-protocol.](#)

### REFERENCES AND NOTES

1. L. A. Malone, M. S. Proctor, A. Hitchcock, C. N. Hunter, M. P. Johnson, Cytochrome  $b_6f$  —Orchestrator of photosynthetic electron transfer. *Biochim. Biophys. Acta Bioenerg.* **1862**, 148380 (2021).

2. M. Sarewicz, S. Pintscher, R. Pietras, A. Borek, Ł. Bujnowicz, G. Hanke, W. A. Cramer, G. Finazzi, A. Osyczka, Catalytic reactions and energy conservation in the cytochrome *bc<sub>1</sub>* and *b<sub>6</sub>f* complexes of energy-transducing membranes. *Chem. Rev.* **121**, 2020–2108 (2021).
3. W. A. Cramer, S. S. Hasan, in *Cytochrome Complexes: Evolution, Structures, Energy Transduction, and Signaling*, W. A. Cramer, T. Kallas, Eds. (Springer, 2016), pp. 177–207.
4. D. M. Kramer, W. Nitschke, J. W. Cooley, in *The Purple Phototrophic Bacteria* (Springer, 2009), pp. 451–473; [http://link.springer.com/10.1007/978-1-4020-8815-5\\_23](http://link.springer.com/10.1007/978-1-4020-8815-5_23).
5. A. N. Tikhonov, The cytochrome *b<sub>6</sub>f* complex at the crossroad of photosynthetic electron transport pathways. *Plant Physiol. Biochem.* **81**, 163–183 (2014).
6. J. F. Allen, Photosynthesis of ATP-electrons, proton pumps, rotors, and poise. *Cell* **110**, 273–276 (2002).
7. W. A. Cramer, T. Kallas, *Cytochrome Complexes-Evolution, Structures, Energy Transduction, and Signaling* (Springer, 2016).
8. S. Al-Attar, S. de Vries, Energy transduction by respiratory metallo-enzymes: From molecular mechanism to cell physiology. *Coord. Chem. Rev.* **257**, 64–80 (2013).
9. P. Mitchell, The protonmotive Q cycle: A general formulation. *FEBS Lett.* **59**, 137–139 (1975).
10. A. R. Crofts, S. W. Meinhardt, K. R. Jones, M. Snozzi, The role of the quinone pool in the cyclic electron-transfer chain of *Rhodospseudomonas sphaeroides*: A modified Q-cycle mechanism. *Biochim. Biophys. Acta* **723**, 202–218 (1983).
11. A. Osyczka, C. C. Moser, P. L. Dutton, Fixing the Q cycle. *Trends Biochem. Sci.* **30**, 176–182 (2005).
12. A. Y. Mulikidjanian, Activated Q-cycle as a common mechanism for cytochrome *bc<sub>1</sub>* and cytochrome *b<sub>6</sub>f* complexes. *Biochim. Biophys. Acta* **1797**, 1858–1868 (2010).
13. W. A. Cramer, S. S. Hasan, E. Yamashita, The Q cycle of cytochrome *bc* complexes: A structure perspective. *Biochim. Biophys. Acta* **1807**, 788–802 (2011).
14. P. Joliot, G. N. Johnson, Regulation of cyclic and linear electron flow in higher plants. *Proc. Natl. Acad. Sci. U.S.A.* **108**, 13317–13322 (2011).
15. W. J. Nawrocki, B. Bailleul, D. Picot, P. Cardol, F. Rappaport, F.-A. Wollman, P. Joliot, The mechanism of cyclic electron flow. *Biochim. Biophys. Acta Bioenerg.* **1860**, 433–438 (2019).
16. J. D. Rochaix, S. Lemeille, A. Shapiguzov, I. Samol, G. Fucile, A. Willig, M. Goldschmidt-Clermont, Protein kinases and phosphatases involved in the acclimation of the photosynthetic apparatus to a changing light environment. *Philos. Trans. R. Soc. B Biol. Sci.* **367**, 3466–3474 (2012).
17. S. S. Hasan, E. Yamashita, W. A. Cramer, Transmembrane signaling and assembly of the cytochrome *b<sub>6</sub>f*-lipidic charge transfer complex. *Biochim. Biophys. Acta* **1827**, 1295–1308 (2013).
18. D. Stroebel, Y. Choquet, J. L. Popot, D. Picot, An atypical haem in the cytochrome *b<sub>6</sub>f* complex. *Nature* **426**, 413–418 (2003).
19. G. Kurisu, H. Zhang, J. L. Smith, W. A. Cramer, Structure of the cytochrome *b<sub>6</sub>f* complex of oxygenic photosynthesis: Tuning the cavity. *Science* **302**, 1009–1014 (2003).
20. L. A. Malone, P. Qian, G. E. Mayneord, A. Hitchcock, D. A. Farmer, R. F. Thompson, D. J. K. Swainsbury, N. A. Ranson, C. N. Hunter, M. P. Johnson, Cryo-EM structure of the spinach cytochrome *b<sub>6</sub>f* complex at 3.6 Å resolution. *Nature* **575**, 535–539 (2019).
21. A. R. Crofts, S. Hong, N. Ugulava, B. Barquera, R. Gennis, M. Guergova-Kuras, E. A. Berry, Pathways for proton release during ubiquinol oxidation by the *bc<sub>1</sub>* complex. *Proc. Natl. Acad. Sci. U.S.A.* **96**, 10021–10026 (1999).
22. M. Ubbink, M. Ejdebäck, B. G. Karlsson, D. S. Bendall, The structure of the complex of plastocyanin and cytochrome *f*, determined by paramagnetic NMR and restrained rigid-body molecular dynamics. *Structure* **6**, 323–335 (1998).
23. C. Lange, T. Cornvik, I. Díaz-Moreno, M. Ubbink, The transient complex of poplar plastocyanin with cytochrome *f*: Effects of ionic strength and pH. *Biochim. Biophys. Acta Bioenerg.* **1707**, 179–188 (2005).
24. I. Díaz-Moreno, R. Hulsker, P. Skubak, J. M. Foerster, D. Cavazzini, M. G. Finiguerra, A. Díaz-Quintana, B. Moreno-Beltrán, G. L. Rossi, G. M. Ullmann, N. S. Pannu, M. A. De La Rosa, M. Ubbink, The dynamic complex of cytochrome *c<sub>6</sub>* and cytochrome *f* studied with paramagnetic NMR spectroscopy. *Biochim. Biophys. Acta Bioenerg.* **1837**, 1305–1315 (2014).
25. C. R. Hackenbrock, B. Chazotte, S. S. Gupte, The random collision model and a critical assessment of diffusion and collision in mitochondrial electron transport. *J. Bioenerg. Biomembr.* **18**, 331–368 (1986).
26. M. Sarewicz, A. Borek, F. Daldal, W. Froncisz, A. Osyczka, Demonstration of short-lived complexes of cytochrome *c* with cytochrome *bc<sub>1</sub>* by EPR spectroscopy: Implications for the mechanism of interprotein electron transfer. *J. Biol. Chem.* **283**, 24826–24836 (2008).
27. C. Lange, C. Hunte, Crystal structure of the yeast cytochrome *bc<sub>1</sub>* complex with its bound substrate cytochrome *c*. *Proc. Natl. Acad. Sci. U.S.A.* **99**, 2800–2805 (2002).
28. W.-C. Kao, C. Hunte, The molecular evolution of the Q<sub>o</sub> motif. *Genome Biol. Evol.* **6**, 1894–1910 (2014).
29. A. I. Zatsman, H. Zhang, W. A. Gunderson, W. A. Cramer, M. P. Hendrich, Heme-heme interactions in the cytochrome *b<sub>6</sub>f* complex: EPR spectroscopy and correlation with structure. *J. Am. Chem. Soc.* **128**, 14246–14247 (2006).
30. E. Yamashita, H. Zhang, W. A. Cramer, Structure of the cytochrome *b<sub>6</sub>f* complex: Quinone analogue inhibitors as ligands of heme c<sub>n</sub>. *J. Mol. Biol.* **370**, 39–52 (2007).
31. W. A. Cramer, H. Zhang, J. Yan, G. Kurisu, J. L. Smith, Transmembrane traffic in the cytochrome *b<sub>6</sub>f* complex. *Annu. Rev. Biochem.* **75**, 769–790 (2006).
32. J. Song, M. S. Lee, I. Carlberg, A. V. Vener, J. L. Markley, Micelle-induced folding of spinach thylakoid soluble phosphoprotein of 9 kDa and its functional implications. *Biochemistry* **45**, 15633–15643 (2006).
33. S. S. Hasan, E. A. Proctor, E. Yamashita, N. V. Dokholyan, W. A. Cramer, Traffic within the cytochrome *b<sub>6</sub>f* lipoprotein complex: Gating of the quinone portal. *Biophys. J.* **107**, 1620–1628 (2014).
34. S. S. Hasan, E. Yamashita, D. Baniulis, W. A. Cramer, Quinone-dependent proton transfer pathways in the photosynthetic cytochrome *b<sub>6</sub>f* complex. *Proc. Natl. Acad. Sci. U.S.A.* **110**, 4297–4302 (2013).
35. E. A. Berry, L.-S. Huang, L. K. Saechao, N. G. Pon, M. Valkova-Valchanova, F. Daldal, X-ray structure of *Rhodobacter capsulatus* cytochrome *bc<sub>1</sub>*: Comparison with its mitochondrial and chloroplast counterparts. *Photosynth. Res.* **81**, 251–275 (2004).
36. D. Birth, W.-C. Kao, C. Hunte, Structural analysis of atovaquone-inhibited cytochrome *bc<sub>1</sub>* complex reveals the molecular basis of antimalarial drug action. *Nat. Commun.* **5**, 4029 (2014).
37. L. Esser, B. Quinn, Y.-F. Li, M. Zhang, M. Elberry, L. Yu, C.-A. Yu, D. Xia, Crystallographic studies of quinol oxidation site inhibitors: A modified classification of inhibitors for the cytochrome *bc<sub>1</sub>* complex. *J. Mol. Biol.* **341**, 281–302 (2004).
38. J. Yan, W. A. Cramer, Molecular control of a bimodal distribution of quinone-analogue inhibitor binding sites in the cytochrome *b<sub>6</sub>f* complex. *J. Mol. Biol.* **344**, 481–493 (2004).
39. M. Sarewicz, Ł. Bujnowicz, S. Bhaduri, S. K. Singh, W. A. Cramer, A. Osyczka, Metastable radical state, nonreactive with oxygen, is inherent to catalysis by respiratory and photosynthetic cytochromes *bc<sub>1</sub>/b<sub>6</sub>f*. *Proc. Natl. Acad. Sci. U.S.A.* **114**, 1323–1328 (2017).
40. J. Yan, G. Kurisu, W. A. Cramer, Intraprotein transfer of the quinone analogue inhibitor 2,5-dibromo-3-methyl-6-isopropyl-*p*-benzoquinone in the cytochrome *b<sub>6</sub>f* complex. *Proc. Natl. Acad. Sci. U.S.A.* **103**, 69–74 (2006).
41. W. Grudzinski, E. Janik, J. Bednarska, R. Welc, M. Zubik, K. Sowinski, R. Luchowski, W. I. Gruszecki, Light-driven reconfiguration of a xanthophyll violaxanthin in the photosynthetic pigment-protein complex LHCII: A resonance raman study. *J. Phys. Chem. B* **120**, 4373–4382 (2016).
42. A. Sek, R. Welc, M. M. Mendes-Pinto, E. Reszczynska, W. Grudzinski, R. Luchowski, W. I. Gruszecki, Raman spectroscopy analysis of molecular configuration forms of the macular xanthophylls. *J. Raman Spectrosc.* **51**, 635–641 (2020).
43. M. Hansson, T. Dupuis, R. Strömquist, B. Andersson, A. V. Vener, I. Carlberg, The mobile thylakoid phosphoprotein TSP9 interacts with the light-harvesting complex II and the peripheries of both photosystems. *J. Biol. Chem.* **282**, 16214–16222 (2007).
44. T. Goss, G. Hanke, The end of the line: Can ferredoxin and ferredoxin NAD(P)H oxidoreductase determine the fate of photosynthetic electrons? *Curr. Protein Pept. Sci.* **15**, 385–393 (2014).
45. M. S. Proctor, L. A. Malone, D. A. Farmer, D. J. K. Swainsbury, F. R. Hawkings, F. Pastorelli, T. Z. Emrich-Mills, C. A. Siebert, C. N. Hunter, M. P. Johnson, A. Hitchcock, Cryo-EM structures of the *Synechocystis* sp. PCC 6803 cytochrome *b<sub>6</sub>f* complex with and without the regulatory PetP subunit. *Biochem. J.* **479**, 1487–1503 (2022).
46. S. Rexroth, D. Rexroth, S. Veit, N. Plohnke, K. U. Cormann, M. M. Nowaczyk, M. Rögner, Functional characterization of the small regulatory subunit PetP from the cytochrome *b<sub>6</sub>f* complex in *Thermosynechococcus elongatus*. *Plant Cell* **26**, 3435–3448 (2014).
47. A. Osyczka, C. C. Moser, F. Daldal, P. L. Dutton, Reversible redox energy coupling in electron transfer chains. *Nature* **427**, 607–612 (2004).
48. D. Baniulis, H. Zhang, T. Zakharova, S. S. Hasan, W. A. Cramer, Purification and crystallization of the cyanobacterial cytochrome *b<sub>6</sub>f* complex. *Methods Mol. Biol.* **684**, 65–77 (2011).
49. E. Romanowska, Isolation of cytochrome *b<sub>6</sub>f* complex from grana and stroma membranes from spinach chloroplasts. *Methods Mol. Biol.* **684**, 53–64 (2011).
50. R. J. Porra, W. A. Thompson, P. E. Kriedemann, Determination of accurate extinction coefficients and simultaneous equations for assaying chlorophylls a and b extracted with four different solvents: Verification of the concentration of chlorophyll standards by atomic absorption spectroscopy. *BBA-Bioenergetics* **975**, 384–394 (1989).
51. S. D. Zakharov, S. Savikhin, Y. Misumi, G. Kurisu, W. A. Cramer, Isothermal titration calorimetry of membrane protein interactions: FNR and the cytochrome *b<sub>6</sub>f* complex. *Biophys. J.* **121**, 300–308 (2022).
52. S. Katoh, I. Shiratori, A. Takamiya, Purification and some properties of spinach plastocyanin. *J. Biochem.* **51**, 32–40 (1962).

53. A. Punjani, J. L. Rubinstein, D. J. Fleet, M. A. Brubaker, CryoSPARC: Algorithms for rapid unsupervised cryo-EM structure determination. *Nat. Methods* **14**, 290–296 (2017).
54. A. Punjani, H. Zhang, D. J. Fleet, Non-uniform refinement: Adaptive regularization improves single-particle cryo-EM reconstruction. *Nat. Methods* **17**, 1214–1221 (2020).
55. S. M. Stagg, A. J. Noble, M. Spilman, M. S. Chapman, ResLog plots as an empirical metric of the quality of cryo-EM reconstructions. *J. Struct. Biol.* **185**, 418–426 (2014).
56. J. Zivanov, T. Nakane, S. H. W. Scheres, Estimation of high-order aberrations and anisotropic magnification from cryo-EM data sets in RELION-3.1. *IUCr* **7**, 253–267 (2020).
57. S. H. W. Scheres, RELION: Implementation of a Bayesian approach to cryo-EM structure determination. *J. Struct. Biol.* **180**, 519–530 (2012).
58. T. Bepler, K. Kelley, A. J. Noble, B. Berger, Topaz-Denoise: General deep denoising models for cryoEM and cryoET. *Nat. Commun.* **11**, 5208 (2020).
59. T. Bepler, A. Morin, M. Rapp, J. Brasch, L. Shapiro, A. J. Noble, B. Berger, Positive-unlabeled convolutional neural networks for particle picking in cryo-electron micrographs. *Nat. Methods* **16**, 1153–1160 (2019).
60. P. Emsley, B. Lohkamp, W. G. Scott, K. Cowtan, Features and development of Coot. *Acta Crystallogr. Sect. D Biol. Crystallogr.* **66**, 486–501 (2010).
61. P. D. Adams, P. V. Afonine, G. Bunkóczi, V. B. Chen, I. W. Davis, N. Echols, J. J. Headd, L.-W. Hung, G. J. Kapral, R. W. Grosse-Kunstleve, A. J. McCoy, N. W. Moriarty, R. Oeffner, R. J. Read, D. C. Richardson, J. S. Richardson, T. C. Terwilliger, P. H. Zwart, PHENIX: A comprehensive Python-based system for macromolecular structure solution. *Acta Crystallogr. Sect. D Biol. Crystallogr.* **66**, 213–221 (2010).
62. I. W. Davis, A. Leaver-Fay, V. B. Chen, J. N. Block, G. J. Kapral, X. Wang, L. W. Murray, W. B. Arendall, J. Snoeyink, J. S. Richardson, D. C. Richardson, MolProbity: All-atom contacts and structure validation for proteins and nucleic acids. *Nucleic Acids Res.* **35**, W375–W383 (2007).
63. J. Rappsilber, M. Mann, Y. Ishihama, Protocol for micro-purification, enrichment, pre-fractionation and storage of peptides for proteomics using StageTips. *Nat. Protoc.* **2**, 1896–1906 (2007).
64. C. S. Hughes, S. Foehr, D. A. Garfield, E. E. Furlong, L. M. Steinmetz, J. Krijgsvelde, Ultra-sensitive proteome analysis using paramagnetic bead technology. *Mol. Syst. Biol.* **10**, 757 (2014).

**Acknowledgments:** We thank all members of the Osyczka and Glatt laboratories for discussion and suggestions. We thank R. Ekiert for assistance with SDS-PAGE analyses. We would like to thank L. P. Dutton and J. Heddle for critical comments on the manuscript draft. We specially thank U. Jankowska and B. Skupień-Rabian from the Proteomics and Mass Spectrometry Core Facility at MCB for their excellent work and support. In particular, we would like to thank all staff at the SOLARIS National Synchrotron Radiation Centre, Poland. **Funding:** This work was supported by the Team grant (POIR.04.04.00-00-5B54/17-00 to A.O.) and the TEAM-TECH Core Facility grant (TEAM TECH CORE FACILITY/2017-4/6 to S.G.) from the Foundation for Polish Science. **Author contributions:** The study was designed and directed by M.Sa., S.G., and A.O. M.Sz., R.P., and B.M. purified the samples and reconstituted the complex. S.P. purified plastocyanin and prepared the MS samples. M.Sa., M.Sz., P.I., S.P., and M.R. prepared the cryo-EM samples and performed initial grid screening and grid optimization. Data collection, data analyses, and data processing were done by M.J., Ł.K., P.I., and M.R. Map interpretation, model building, and refinement were done by S.P., Ł.K., M.J., and S.G. with constant feedback from all authors. M.Sa. performed the EPR experiments. M.Sz. and S.P. performed optical spectrophotometry and biochemical characterization of the proteins. Figures were prepared by M.Sa., M.Sz., S.P., M.J., and M.R. with the support of S.G. and A.O. The manuscript was written by M.Sa., S.G., and A.O., with all authors discussing the results and refining and approving the final version of it. **Competing interests:** The authors declare that they have no competing interests. **Data and materials availability:** The atomic models of Cyt b<sub>6</sub>f-PC and Cyt b<sub>6</sub>f (PDB ID: 7QRN and 7ZYV, respectively), cryo-EM densities (EMD-14123 and EMD-15027, respectively) and raw data (EMPIAR-11347) have been deposited in the EMDData Bank (EMDB), the PDB and the Electron Microscopy Public Image Archive (EMPIAR). All data needed to evaluate the conclusions in the paper are present in the paper and/or the Supplementary Materials.

Submitted 15 July 2022

Accepted 14 December 2022

Published 13 January 2023

10.1126/sciadv.add9688